

Possibility of mechanical fracture of superconducting ring bulks due to thermal stress induced by local heat generation during pulsed-field magnetization

Motoki Shinden¹, Hiroyuki Fujishiro^{1,*} , Keita Takahashi²  and Mark D Ainslie³ 

¹ Department of Physical Science and Materials Engineering, Faculty of Science and Engineering, Iwate University, 4-3-5 Ueda, Morioka 020-8551, Japan

² Department of Physics, Faculty of Science, Gakushuin University, 1-5-1 Mejiro, Toshima, Tokyo 171-8588, Japan

³ Department of Engineering, University of Cambridge, Trumpington Street, Cambridge CB2 1PZ, United Kingdom

E-mail: fujishiro@iwate-u.ac.jp

Received 25 October 2021, revised 17 February 2022

Accepted for publication 22 February 2022

Published 4 March 2022



CrossMark

Abstract

During quasi-static magnetization of bulk superconductors using field-cooled magnetization (FCM) from high fields at low temperatures, such bulks are sometimes broken, which is believed to be mainly due to an electromagnetic force—and subsequent stress—larger than the fracture strength. However, a ring bulk can break, even during pulsed field magnetization (PFM), from relatively lower pulsed fields and at relatively higher temperatures. Previous simulation results suggest that the ring bulk should not break due to the electromagnetic force during PFM. In this paper, taking experimental and numerical results into consideration, we propose the possibility of mechanical fracture of a ring bulk during PFM due to thermal stress induced by local heat generation, which has not been considered and investigated to date. Two numerical models with different sizes of heat-generating region were constructed for the ring bulk with a relatively large inner diameter (60 mm outer diameter, 36 mm inner diameter, 17 mm height). For Model-1, with a large heat region, the bulk fracture due to the thermal stress results from the tensile stress along the radial direction in the neighboring heat region. The risk of bulk fracture is enhanced at the inner or outer edges of the bulk surface, compared with that inside the bulk. For Model-2, with a small heat region inside the bulk, the bulk fracture due to the thermal stress results from the compressive stress along the radial direction in the neighboring heat region. These results strongly suggest the possibility of mechanical fracture of an actual ring bulk due to thermal stress induced by local heat generation. This idea is also applicable more generally to the fracture mechanism during FCM of superconducting bulks.

Keywords: mechanical fracture, thermal stress, superconducting ring bulk, flux jump, numerical simulation, pulsed field magnetization, local heat generation

(Some figures may appear in colour only in the online journal)

* Author to whom any correspondence should be addressed.

1. Introduction

A superconducting bulk can be used as trapped field magnet in applications such as motors and generators [1], magnetic separation [2] and nuclear magnetic resonance (NMR) [3]. In particular, REBaCuO superconducting bulks (RE: rare earth element or Y) exhibit a superior temperature and magnetic field dependence of critical current density, $J_c(T, B)$, which have resulted in trapped fields, B_T^{FCM} , over 17 T in disk bulk pairs by field-cooled magnetization (FCM) [4–6].

In addition, pulsed-field magnetization (PFM) has been intensively investigated as a compact, mobile and relatively inexpensive magnetizing technique, in which a magnetic pulse as short as several milliseconds is applied to the bulk cooled below its critical temperature, T_c . However, the trapped field by PFM, B_T^{PFM} , is often much lower than B_T^{FCM} because of a large temperature rise due to the dynamical motion of the magnetic flux in the bulk. Various studies on PFM techniques have been performed to reduce the temperature rise and to enhance the B_T^{PFM} value [7, 8]. At present, the maximum record of B_T^{PFM} is 5.2 T at 29 K for an Ag-containing GdBaCuO disk bulk 45 mm in diameter magnetized by the modified multi-pulse technique combined with stepwise cooling [9] and 5.3 T at 30 K between a stack of two Ag-containing GdBCO disk bulks 30 mm in diameter using an optimized two-step pulse sequence [10]. However, for a ring bulk, only a small B_T^{PFM} has been observed to date [11, 12]. For example, B_T^{PFM} of 0.25 T was achieved at 60 K for the GdBaCuO ring bulk (30 mm in outer diameter (O.D.), 12 mm in inner diameter (I.D.) and 12 mm in height (H)), because flux jumps readily occur, even for relatively lower applied pulsed fields [13].

Since REBaCuO bulk materials are intrinsically a brittle ceramic material, the mechanical strength, especially the tensile strength, is fairly low. The mechanical strength of bulk materials has typically been measured by bending tests [14–16] and tensile tests [17, 18], from which the fracture strength of tensile stress is suggested to be as low as 50–70 MPa for a typical Ag-doped REBaCuO bulk [19]. The fracture strength of the REBaCuO bulk for compressive stress was reported to be at least –200 MPa [20, 21]. A large tensile stress (or hoop stress) due to the Lorentz force is generated in the bulk during FCM, especially for fields higher than several tesla, which sometimes creates a crack and eventually mechanical failure. To avoid mechanical fracture, mechanical reinforcement is usually applied by shrink-fit stainless steel or epoxy resin impregnation [4, 5].

On the other hand, for PFM, the compressive and tensile stresses are generated in the bulk during the ascending and descending stages of PFM, respectively. The magnitude of the electromagnetic stress is relatively low, compared with that for the FCM process, because the strength of the applied field and resultant trapped field is lower and $J_c(T, B)$ is reduced due to the heat generated. As a result, there is no report of mechanical fracture of a disk bulk during the PFM process, as far as the authors' knowledge. However, during the PFM of ring bulks, mechanical fracture has been observed, in addition to

the local overheating and the destruction of superconductivity due to flux jumps. We have performed PFM experiments on a GdBaCuO ring bulk with a relatively large I.D. (60 mm in O.D., 36 mm in I.D., 17 mm in H) for an applied field $B_{\text{app}} = 3.10$ T at 65 K [22]. A flux jump took place during the ascending stage of the pulse, and the final trapped field had a negative value and exhibited a 'C-shaped' trapped field profile. After the PFM experiment, a mechanical fracture was confirmed by examining the trapped field profile by FCM in liquid nitrogen.

The mechanical properties have been analyzed for superconducting bulks with an infinite height during FCM and zero-field-cooled magnetization [23–25]. We have also investigated the mechanical properties of disk- and ring-shaped REBaCuO bulks with finite height during FCM using the finite element method (FEM) and proposed optimal reinforcement structures made of metal to avoid mechanical fracture [19, 26–29]. For PFM, FEM analyses of mechanical properties have been performed such as quench and crack propagation in the disk bulk [30–34]. We have also investigated the electromagnetic and thermal properties of REBaCuO ring bulks with an inhomogeneous critical current density, J_c , profile during PFM using numerical simulations, and compared these with those of a ring bulk with a homogeneous J_c profile [35], in which the electromagnetic and thermal hoop stresses were lower than the fracture strength of the bulk material. These simulation results suggest that the experimentally observed 'C-shaped' profile does not result from the bulk fracture, but rather from the disconnect of the circulating supercurrent by a thermally-induced flux jump. However, the ring bulk was actually broken during PFM, even for lower B_{app} and a higher operating temperature, T_s [22]. We must consider another cause of the mechanical fracture of the ring bulk during PFM. In a previous study, the flux penetration promotes the local temperature rise, which is estimated to be higher than T_c [35]. The results strongly suggest the possibility of the mechanical fracture due not to the electromagnetic hoop stress, but rather the local thermal stress related to the flux jump. Such a proposal, and related investigations, have not yet been considered in the literature.

In this paper, the possibility of mechanical fracture of a superconducting ring bulk due to thermal stress induced by local heat generation during the PFM process was investigated numerically. First, PFM experiments on a GdBaCuO ring bulk were performed, for which the mechanical fracture was confirmed again, similar to our previous experiments [22]. Second, to clarify the influence of local heat generation on the mechanical fracture of the ring bulk, two numerical models with different sizes of heat-generating region are constructed and the thermal stress is investigated for each case, in which the electromagnetic stress is not considered. As a result, the possibility of mechanical fracture of a superconducting ring bulk specifically due to thermal stress during PFM is strongly suggested. The proposed fracture mechanism due to thermal stress is also applicable to the bulk fracture during FCM, for which only an electromagnetic origin has mainly been considered.

2. Experimental procedure

2.1. Experimental setup and FCM process

The experimental PFM apparatus and procedure are described elsewhere in detail [36]. The GdBaCuO superconducting ring bulk (60 mm in O.D., 36 mm in I.D., 17 mm in H), fabricated by Nippon Steel, Japan, was thermally connected to the cold stage of a GM-cycle helium refrigerator and then evacuated in a vacuum chamber. The temperature of the cold stage was controlled at $T_s = 40$ K using a Pt/Co thermometer and resistive heater. A magnetic pulse, $B_{ex}(t)$, was applied to the bulk using a solenoid-type copper coil set outside the vacuum chamber and a capacitor bank. The peak of $B_{ex}(t)$ is defined as B_{app} , and the rise time and duration time are $t_r = 13$ ms and $t_d = 200$ ms, respectively. The time dependence of $B_{ex}(t)$ was monitored from the current $I(t)$ flowing in a shunt resistor. The time evolution of the magnetic field, $B_z(t)$, was measured at the bore center of the ring bulk using an axial-type Hall sensor (F. W. Bell, BHA-921). The time dependence of the temperature, $T(t)$, was measured on the side surface of the stainless steel holder of the ring bulk using a Cernox thermometer.

After the PFM process at $T_s = 40$ K, a two-dimensional trapped field profile of B_z was mapped at 3 mm above the ring bulk surface in the vacuum chamber by scanning the same Hall sensor using an x - y stage controller. To confirm the mechanical fracture, the ring bulk was removed from the apparatus, then the bulk was magnetized by FCM from 1.5 T in liquid nitrogen and a two-dimensional trapped field profile of B_z was mapped at 1 mm above the ring bulk surface at 77 K.

3. Numerical simulation framework

We constructed a three-dimensional (3D) numerical model for a REBaCuO ring bulk (60 mm in O.D., 36 mm in I.D., 16 mm in H), of a similar size as the experiment. The commercial software package, Photo-Thermo-Elas (Photon Ltd, Japan), was used for analyses of the thermal and mechanical properties. The model was equally divided every 1° along the circumferential (φ) direction and every 1 mm along the radial (r)- and central axis (z)-directions. Figure 1(a) shows the top view of the simulation model. The azimuth angle, φ , was defined as shown in the figure and the heat region was set between 89° and 92° (totaling 3°). In this study, two types of heat region were assumed, named Model-1 and Model-2, as shown in figures 1(b) and (c), in which the heat power was induced forcibly. Model-1 was constructed based on the previous results showing the ‘C-shaped’ trapped field profile [22], as shown in figure 1(b), where the heat region was $18 \leq r \leq 30$ mm, $89 \leq \varphi \leq 92^\circ$ and $-8 \leq z \leq 8$ mm. The number of mesh elements within the heat region is 576, which is 1/120 of the total mesh. Model-2 was constructed as a local and small heat region, as shown in figure 1(c), where the heat region was $22 \leq r \leq 25$ mm, $89 \leq \varphi \leq 92^\circ$ and $-1 \leq z \leq 2$ mm. The number of mesh elements in the heat region is 27, which is about 1/21 of that of Model-1. As thermal and mechanical boundary conditions, the modeled bulk was assumed not to contact

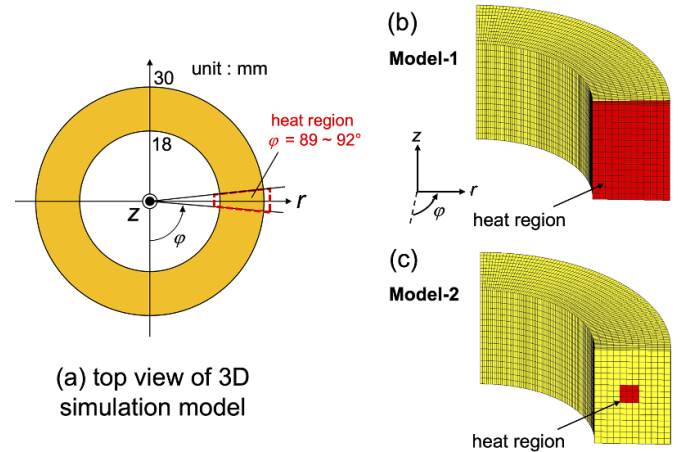


Figure 1. Schematic views of the numerical models for the ring bulk: (a) top view of the 3D simulation model. (b) Model-1, where a large heat region (red) is defined at $18 \leq r \leq 30$ mm, $89 \leq \varphi \leq 92^\circ$, and $-8 \leq z \leq 8$ mm. (c) Model-2, where a local and small heat region (red) is defined at $22 \leq r \leq 25$ mm, $89 \leq \varphi \leq 92^\circ$ and $-1 \leq z \leq 2$ mm (see text).

anywhere, and to be thermally insulated (adiabatic) and mechanically ‘floating’.

Elastic behavior in an isotropic material is expressed by Hooke’s law [26], in which the stress tensor, σ_{ij} , is linearly proportional to the strain tensor, ε_{ij} , as follows,

$$\sigma_{ij} = \lambda \cdot \varepsilon_{kk} \cdot \delta_{ij} + 2G \cdot \varepsilon_{ij}, \quad (1)$$

$$\lambda = \frac{E \cdot \nu}{(1 + \nu)(1 + 2\nu)}, \quad (2)$$

$$G = \frac{E}{2(1 + \nu)}, \quad (3)$$

where λ and G are the Lamé’s constants, δ_{ij} is the Kronecker delta function, E ($=100$ GPa) is the Young’s modulus, and ν ($=0.33$) is the Poisson ratio of the GdBaCuO bulk material. The thermal expansion coefficient, α_0 , of the bulk material is assumed to be $5.2 \times 10^{-6} \text{ K}^{-1}$. All the mechanical parameters were used in our previous simulation studies [26, 37, 38].

In this study, the maximum temperature, T_{max} , of the heat region for each model was assumed as 90 K, 140 K, 200 K, 250 K and 300 K. The induced heat, Q , which was required to raise up to T_{max} from $T_s = 40$ K, was calculated using the following equation,

$$Q = \int_{T_s=40 \text{ K}}^{T_{max}} C(T) V_{\text{heat}} dT, \quad (4)$$

where V_{heat} is the volume of the heat region for each model. $C(T)$ ($\text{J (m}^3\text{K)}^{-1}$) is the temperature dependence of the specific heat, for which the measured $C(T)$ [39] was approximated using the following 6th degree polynomial equation. The parameters, a_0 to a_6 , in equation (5) are shown in table 1. The temperature dependence of thermal conductivity, $\kappa(T)$, was referred from [40].

Table 1. Fitting parameters for equation (5).

Parameter	a_0	a_1	a_2	a_3	a_4	a_5	a_6
	1.513×10^3	-4.431×10^3	4.955×10^2	-5.565×10^0	2.869×10^{-2}	-7.153×10^{-5}	6.943×10^{-8}

$$C(T) = a_0 + a_1T + a_2T^2 + a_3T^3 + a_4T^4 + a_5T^5 + a_6T^6 \quad (5)$$

As shown in the next section, a flux jump, i.e. an abrupt flux intrusion and related heat generation, took place at $t = 5$ ms. For $t < 5$ ms, a shielding current, I_{shield} , flows in the ring bulk and increases monotonically with increasing time [41], at which there is no heat generation. In the present numerical simulation, to realize the convergence of the calculation, we assume that the heat power q (W m^{-3}) is applied to the heat region and then the temperature increases between 0 and 5 ms and reaches T_{max} , which may be slightly different to the actual phenomenon. As a result, a local thermal stress must be generated due to the local thermal expansion difference between heat region and its neighboring region. The thermal stress increases with time for $0 < t < 5$ ms, and then decreases for $t > 5$ ms because $q = 0$ for $t > 5$ ms. In this study, the thermal stress along the radial (r) direction, σ_r^{heat} , and that along the circumferential (φ) direction, $\sigma_\varphi^{\text{heat}}$, were investigated at each T_{max} at $t = 5$ ms for the heat region ($89^\circ < \varphi < 92^\circ$) and neighboring regions ($\varphi < 89^\circ$, $\varphi > 92^\circ$) for each model. Korotokov and Brazhnik calculated the shielding current, I_{shield} , from which the electromagnetic energy, $Q = LI_{\text{shield}}^2/2$, accumulated in the bulk was released to the heat region by the flux jump [41–43], where L is the inductance of the ring bulk. Based on the results of Korotokov and Brazhnik [41, 44], we calculated I_{shield} for each T_{max} and for each model, where the L value in the present ring bulk was estimated to be $L = 1.048 \times 10^{-7}$ H.

4. Experimental results

Figure 2(a) presents the time dependence of the applied pulsed field, $B_{\text{ex}}(t)$, and trapped field, $B_{\text{center}}(t)$, at the bore center of the ring bulk for $T_s = 40$ K and $B_{\text{app}} = 3.88$ T. $B_{\text{center}}(t)$ was zero for $0 \leq t \leq 5$ ms due to flux shielding and then abruptly increased with time for $t > 5$ ms. After that, $B_{\text{center}}(t)$ was larger than $B_{\text{ex}}(t)$, took a maximum, and then became negative ($= -0.08$ T) at $t = 200$ ms. The final negative value suggests the disconnection of the circulating supercurrent in the bulk [22, 35, 42]. The characteristic result of $B_{\text{center}}(t) > B_{\text{ex}}(t)$ comes from the so-called ‘magnetic lens effect’ [45, 46], which appeared due to the disconnection of circulating supercurrent as pointed out by Brazhnik [44]. Figure 2(b) shows the trapped field profile 3 mm above the bulk surface after PFM. The ‘C-shaped’ trapped field profile was observed. At this stage, we cannot conclude the origin of the ‘C-shaped’ trapped field profile, i.e. whether it is due to thermal disconnection of the circulating supercurrent or mechanical fracture of the ring bulk.

After that, the bulk was warmed above T_c to release the trapped field, and then cooled to $T_s = 40$ K again. Figure 2(c) shows the time dependence of $B_{\text{ex}}(t)$ and $B_{\text{center}}(t)$ at the bore

center of the ring bulk for $B_{\text{app}} = 3.49$ T. The magnetic shielding effect is not observed at $t < 5$ ms and $B_{\text{ex}}(t)$ and $B_{\text{center}}(t)$ overlapped fully. $B_{\text{center}}(t)$ at $t = 200$ ms was negative ($= -0.05$ T) similar to figure 2(a). These results also indicate the disconnection of circulating supercurrent and suggest that the ring bulk was broken during the first pulse application. An FCM experiment was performed from $B_{\text{app}} = 1.5$ T at 77 K. Figure 2(d) presents the trapped field profile at 1 mm above the ring bulk. The ‘C-shaped’ trapped field profile was confirmed, which suggests the bulk fracture with good certainty. We concluded that the present ring bulk was fractured at around $t = 5$ ms during the first pulse application ($B_{\text{app}} = 3.88$ T) at 40 K.

Our group previously investigated the electromagnetic and thermal properties of a REBaCuO ring bulk with an inhomogeneous J_c profile during PFM using numerical simulations [35], in which $B_{\text{app}} = 4.0$ T was applied at $T_s = 65$ K. The calculated compressive electromagnetic stress and tensile thermal stress were lower than the fracture strength of the bulk material, suggesting that the experimentally observed ‘C-shaped’ profile resulted from a (thermomagnetic) flux jump, rather than the bulk fracture. However, the present ring bulk was actually broken. We must consider a cause of this fracture other than that of an electromagnetic origin.

5. Numerical results and discussion

5.1. Induced heat Q to reach the maximum temperature T_{max}

First, the induced heat, Q , to reach a maximum temperature, T_{max} , of 90 K, 140 K, 200 K, 250 K and 300 K in each model was estimated. The heat power q (W m^{-3}) was applied to the heat region for 5 ms to reach each T_{max} . Figure 3(a) shows the time dependence of the temperature, T , to reach $T_{\text{max}} = 140$ K and 300 K for Model-1. When a heat power of $q = 8.21 \times 10^{10}$ (W m^{-3}) was applied for 5 ms to the heat region ($V_{\text{heat}} = 2.56 \times 10^{-7}$ m³), the temperature of the heat region increased monotonically with time and became $T_{\text{max}} = 300$ K at $t = 5$ ms. In this case, the total induced heat was $Q = qV_{\text{heat}}t = 105$ J. When a heat power of $q = 2.20 \times 10^{10}$ (W m^{-3}) was applied for 5 ms to the heat region, the total induced heat was $Q = qV_{\text{heat}}t = 25.8$ J and the temperature became $T_{\text{max}} = 140$ K at $t = 5$ ms. The mechanical results after this are shown at T_{max} ($t = 5$ ms).

Figure 3(b) shows the relationship between T_{max} and Q for each model. T_{max} increases with increasing Q for each model with a nearly square root dependence of T_{max} on Q , i.e. $T_{\text{max}} \sim Q^{1/2}$. The Q value in Model-1 is 21 times as large as that in Model-2 to reach the same T_{max} because of the same ratio of V_{heat} for the two models. The temperature was confirmed to rise from 40 K to 46 K for PFM with $B_{\text{app}} = 3.88$ T, as shown in figure 2(a). In this case, the estimated heat generation—using

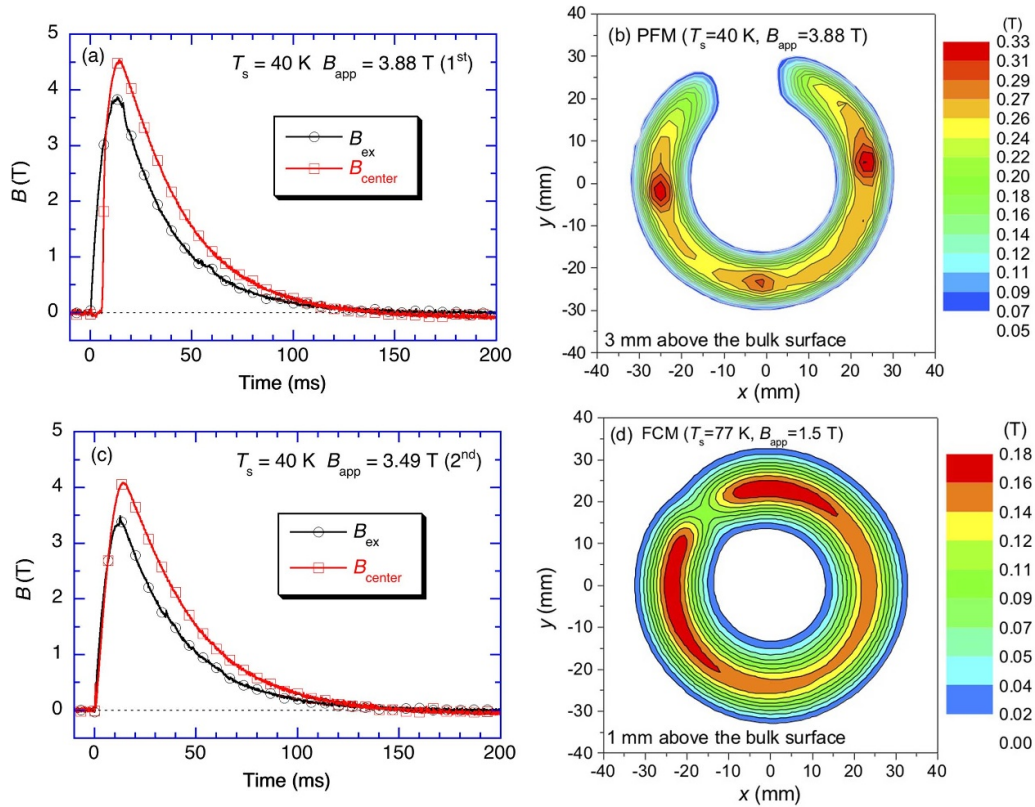


Figure 2. (a) Time dependence of the applied pulsed field, $B_{ex}(t)$, and trapped field, $B_{center}(t)$, at the bore center of the ring bulk for $B_{app} = 3.88$ T (1st pulse). (b) Trapped field profile 3 mm above the bulk surface after PFM. (c) Time dependence of $B_{ex}(t)$ and $B_{center}(t)$ at the bore center of the ring bulk for $B_{app} = 3.49$ T (2nd pulse). (d) Final trapped field profile of the ring bulk 1 mm above the bulk surface by FCM from $B_{app} = 1.5$ T at 77 K.

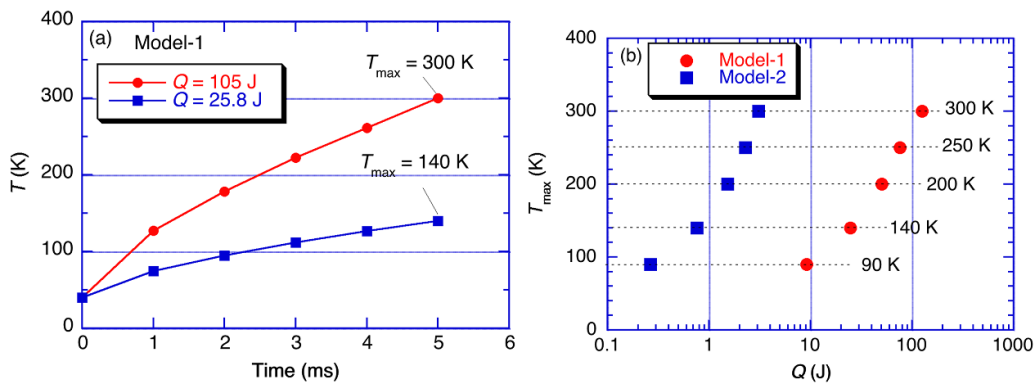


Figure 3. (a) Time dependence of the temperature, T , to reach maximum temperatures, $T_{max} = 140$ K and 300 K for Model-1. (b) The relationship between T_{max} and induced heat, Q , for each model.

equation (4) and $C(T)$ of the ring bulk and its support ring—was 141 J. These results suggest that the local temperature in the bulk could possibly increase above 300 K, if most of the heat power is released in the local heat region.

5.2. Angular dependence of thermal stress for Model-1

Figures 4(a) and (b) show the angular (φ) dependence of the thermal stress along the r -direction, σ_r^{heat} , and along the φ -direction, σ_φ^{heat} , in the bulk ($r = 24$ mm, $z = 0$ mm) for each

T_{max} for Model-1. In the heat region ($\varphi = 89 \sim 92^\circ$), both thermal stresses were negative, i.e. compressive stress. Each thermal compressive stress increases with increasing T_{max} ; σ_r^{heat} was over -100 MPa at $T_{max} = 300$ K. However, σ_φ^{heat} is about one order of magnitude smaller than σ_r^{heat} . This may come from the possibility of displacement in the heat region in Model-1 with open ends along the r - and z -directions. On the other hand, σ_r^{heat} and σ_φ^{heat} for the neighboring regions ($\varphi < 89^\circ, \varphi > 92^\circ$) are positive, i.e. tensile stress, and increase with increasing T_{max} .

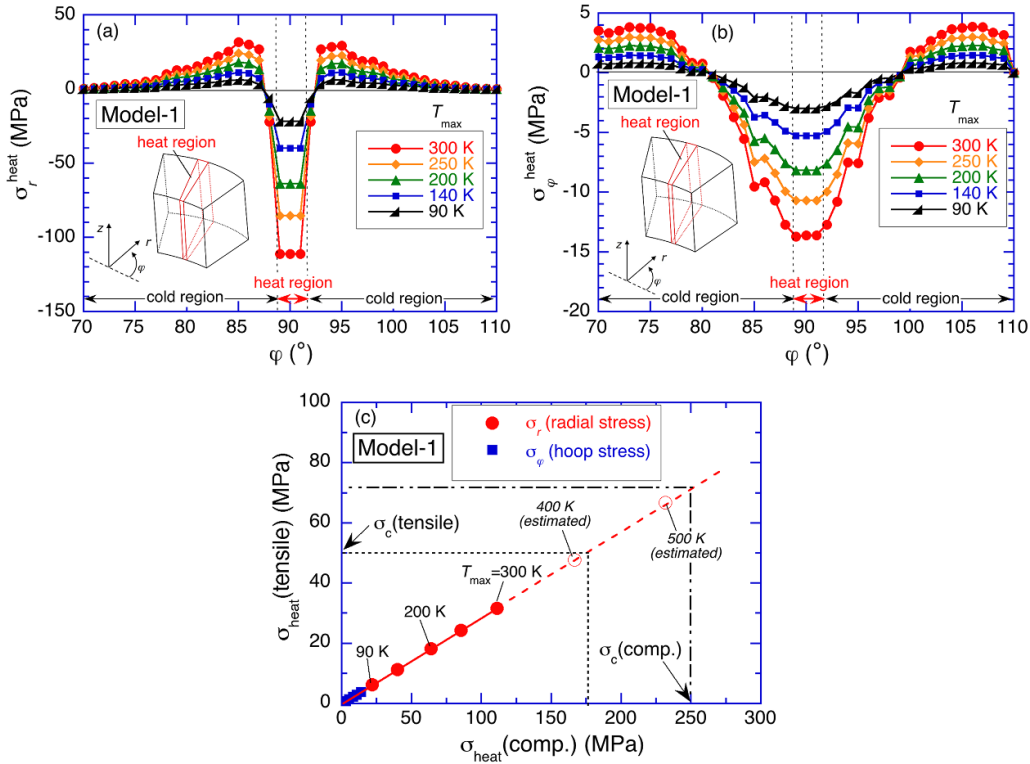


Figure 4. Angular (φ) dependence of thermal stress along (a) the r -direction, σ_r^{heat} , and (b) the φ -direction, $\sigma_\varphi^{\text{heat}}$, in the bulk ($r = 24$ mm, $z = 0$ mm) for each T_{max} for Model-1. (c) The relationship between the maximum thermal compressive stress, $\sigma_{\text{heat}}(\text{comp.})$, and the maximum thermal tensile stress, $\sigma_{\text{heat}}(\text{tensile})$, for σ_r^{heat} and $\sigma_\varphi^{\text{heat}}$ for each T_{max} . The data above 300 K are extrapolated to higher temperatures. The fracture strength in tension, $\sigma_c(\text{tensile}) = 50$ MPa, and in compression, $\sigma_c(\text{comp.}) = 250$ MPa, are indicated.

Figure 4(c) shows the relationship between the maximum thermal compressive stress, $\sigma_{\text{heat}}(\text{comp.})$, in the heat region and the maximum thermal tensile stress, $\sigma_{\text{heat}}(\text{tensile})$, in the neighboring region for σ_r^{heat} shown in figure 4(a) and $\sigma_\varphi^{\text{heat}}$ shown in figure 4(b) for each T_{max} . The data above 300 K are extrapolated to the higher temperatures. The fracture strength in tension, $\sigma_c(\text{tensile})$, for a typical Ag-doped REBaCuO bulk was as low as 50–70 MPa [19], and that in compression, $\sigma_c(\text{comp.})$, was reported to be at least -200 MPa [20, 21]. In this study, the fracture strength in tension, $\sigma_c(\text{tensile}) = 50$ MPa, and in compression, $\sigma_c(\text{comp.}) = 250$ MPa, were adopted as typical values. $\sigma_{\text{heat}}(\text{tensile})$ is linearly proportional to $\sigma_{\text{heat}}(\text{comp.})$ along both directions and the maximum thermal stress along the r -direction is larger, compared with that along the φ -direction. In the case that $\sigma_r(\text{tensile})$ reaches $\sigma_c(\text{tensile}) = 50$ MPa, it is necessary to increase the temperature as high as 400 K. In the case that $\sigma_r(\text{comp.})$ reaches $\sigma_c(\text{comp.}) = 250$ MPa, it is necessary to increase the temperature higher than 500 K. For the thermal stress along the y -direction, it is difficult to reach the fracture strength for tensile and compressive stresses. When the flux jump and the subsequent bulk fracture happened for REBaCuO bulk during FCM, the trace of burning was confirmed at the fracture position [47]. The results suggest that the temperature could raise several hundreds of kelvin and the estimation of the temperature rise seems reasonable. In Model-1, the bulk fracture due to the thermal stress results from the

tensile stress, $\sigma_{\text{heat}}(\text{tensile})$, along the r -direction in the neighboring region, if such fracture happens inside of the ring bulk.

5.3. Influence of an open-end in the heat region on the thermal stress in Model-1

In Model-1, open ends exist in the heat region along the r - and z -directions. In this subsection, the thermal stress at the open ends in the heat region is investigated. As shown in figure 5(a), the cross-sections of the center of the heat region ($\varphi = 90^\circ$), Ω_{heat} , and of the neighboring region ($\varphi = 95^\circ$), Ω_{cool} , were defined. The thermal stress profiles, σ_r^{heat} along the r -direction and $\sigma_\varphi^{\text{heat}}$ along the φ -direction, were mapped at $T_{\text{max}} = 300$ K for each cross-section. Figures 5(b) and (c) show the σ_r^{heat} and $\sigma_\varphi^{\text{heat}}$ profiles in Ω_{heat} and figures 5(d) and (e) show the σ_r^{heat} and $\sigma_\varphi^{\text{heat}}$ profiles in Ω_{cool} , respectively.

Let us consider the thermal stress along the r -direction for each cross-section first. σ_r^{heat} in Ω_{heat} in figure 5(b) indicates a compressive stress in all regions of Ω_{heat} ($\sigma_r < 0$) and negatively increases as we approach the bulk center. On the other hand, σ_r^{heat} in Ω_{cool} in figure 5(d) indicates a tensile stress in all regions of Ω_{cool} ($\sigma_r > 0$). This trend reproduces the result in figure 4(c). Next, we consider the thermal stress along the circumferential direction. At the outer surface of Ω_{heat} , a tensile stress exists ($\sigma_\varphi > 0$), as shown in figure 5(c), and $\sigma_\varphi = 80$ MPa was concentrated at the outer top surface ($r = 18, 30$ mm, $\varphi = 90^\circ$, $z = \pm 8$ mm). In Ω_{cool} , as shown in figure 5(e),

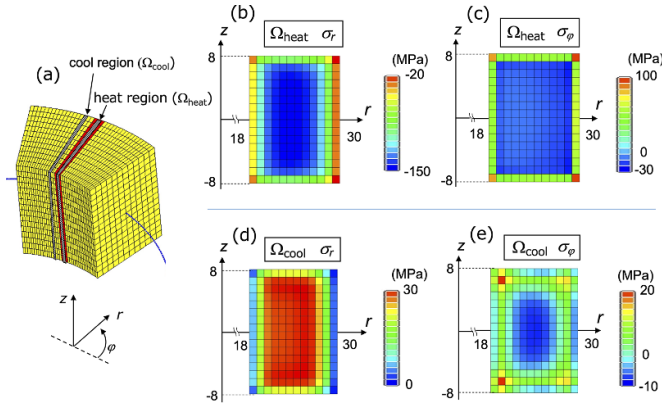


Figure 5. (a) Schematic view of the cross-sections of the center of the heat region ($\varphi = 90^\circ$), Ω_{heat} , and of the neighboring region ($\varphi = 95^\circ$), Ω_{cool} , for Model-1. The thermal stress profiles of (b) σ_r^{heat} and (c) $\sigma_\varphi^{\text{heat}}$ in Ω_{heat} . The thermal stress profiles of (d) σ_r^{heat} and (e) $\sigma_\varphi^{\text{heat}}$ in Ω_{cool} at $T_{\text{max}} = 300$ K for Model-1.

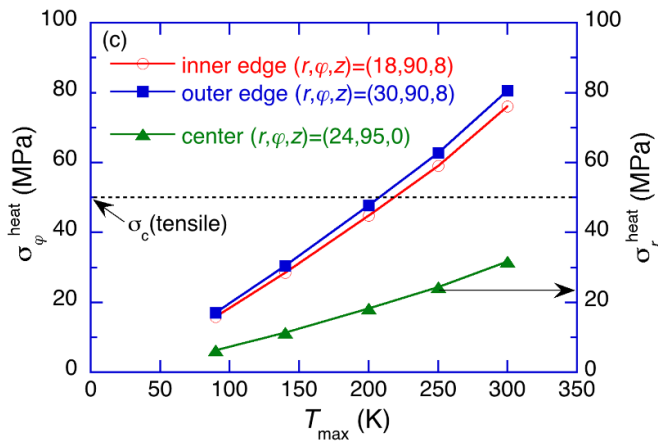


Figure 6. The circumferential tensile stress, $\sigma_\varphi^{\text{heat}}$, at the inner edge ($r = 18$ mm, $\varphi = 90^\circ$, $z = 8$ mm) and the outer edge ($r = 30$ mm, $\varphi = 90^\circ$, $z = 8$ mm) of the heat region in Model-1, as a function of T_{max} . σ_r^{heat} for the neighboring region ($r = 24$ mm, $\varphi = 95^\circ$, $z = 0$ mm) is also shown, which was extracted from figure 4(c).

the strength of σ_φ was moderate at the top/bottom and outer/inner surface regions.

Figure 6 shows the circumferential tensile stress, $\sigma_\varphi^{\text{heat}}$, at the inner edge ($r = 18$ mm, $\varphi = 90^\circ$, $z = 8$ mm) and outer edge ($r = 30$ mm, $\varphi = 90^\circ$, $z = 8$ mm) of the heat region in Model-1, as a function of T_{max} . σ_r^{heat} for the neighboring region ($r = 24$ mm, $\varphi = 95^\circ$, $z = 0$ mm), which is extracted from figure 4, is also shown. It should be noted that $\sigma_\varphi^{\text{heat}}$ at the inner and outer edges of the heat region reaches $\sigma_c^{\text{tensile}}$ even around 200 K. In figure 4(c), we concluded that the bulk fracture due to the thermal stress, σ_r^{heat} , results from the tensile stress in the neighboring region, where a temperature rise higher than 400 K was necessary to break the bulk from inside. These results suggest that the risk of bulk fracture is enhanced at the edge of the bulk surface, rather than inside the bulk.

The induced heat Q was estimated to be 53 J in the case that the temperature rises from $T_s = 40$ K to $T_{\text{max}} = 200$ K using

equation (4). The shielding current, I_{shield} , was also estimated to be 3.1×10^4 A using the relation of $Q = LI_{\text{shield}}^2/2$. I_{shield} flowing in the GdBaCuO ring bulk was experimentally measured to be $1.6\text{--}2.1 \times 10^4$ A at 77 K [26]. Since I_{shield} for the present case, which is for a lower T_s and larger cross section of the ring bulk, is larger than that for the reported case in [41], such local heat generation due to inductance loss at the surface could take place during PFM.

5.4. Angular dependence of thermal stress for Model-2

In this subsection, the angular dependence of the thermal stress for Model-2 is described, in a similar way as for Model-1. Figures 7(a) and (b), respectively, show the φ dependence of the thermal stress along the r -direction, σ_r^{heat} , and along the y -direction, $\sigma_\varphi^{\text{heat}}$, in the bulk ($r = 24$ mm, $z = 0$ mm) for each T_{max} . Each thermal compressive stress increases with increasing T_{max} in the heat region ($\varphi = 89^\circ\text{--}92^\circ$). The compressive σ_r^{heat} along the r -direction shown in figure 7(a) is similar to that for Model-1 in figure 4(a). However, the compressive $\sigma_\varphi^{\text{heat}}$ along the φ -direction in the heat region shown in figure 7(b) is six times larger than that in figure 4(b) for Model-1. $\sigma_\varphi^{\text{heat}}$ along the φ -direction in the neighboring region ($\varphi < 89^\circ$, $\varphi > 92^\circ$) was nearly zero. The heat region in Model-2 exists inside the ring bulk, where the mechanical displacement due to thermal stress is restricted in all directions, which results in the difference in thermal stress between Model-1 and Model-2.

Figure 7(c) shows the relationship between the maximum thermal compressive stress, $\sigma_{\text{heat}}(\text{comp.})$, in the heat region and the maximum thermal tensile stress, $\sigma_{\text{heat}}(\text{tensile})$, in the neighboring region for σ_r^{heat} shown in figure 7(a) and for $\sigma_\varphi^{\text{heat}}$ shown in figure 7(b) for each T_{max} . Again, the data above 300 K are extrapolated to higher temperatures. $\sigma_{\text{heat}}(\text{tensile})$ is nearly proportional to $\sigma_{\text{heat}}(\text{comp.})$ along the r -direction. In the case that $\sigma_{\text{heat}}(\text{comp.})$ reaches $\sigma_c(\text{comp.}) = 250$ MPa and $\sigma_{\text{heat}}(\text{tensile})$ reaches $\sigma_c(\text{tensile}) = 50$ MPa for each direction, it is necessary to increase the temperature higher than 500 K. However, $\sigma_{\text{heat}}(\text{tensile})$ along the y -direction is nearly zero in the neighboring region, contrary to Model-1. The relationship in figure 7(c) suggests that the $\sigma_{\text{heat}}(\text{comp.})$ value along the r -direction reaches $\sigma_c^{\text{comp.}} = 250$ MPa in the heat region with increasing T_{max} , before the $\sigma_{\text{heat}}(\text{tensile})$ value along the r -direction reaches $\sigma_c^{\text{tensile}} = 50$ MPa in the neighboring region. That is, in Model-2, the bulk fracture due to thermal stress results from the compressive stress, $\sigma_{\text{heat}}(\text{comp.})$, along the r -direction in the neighboring region.

We consider the thermal stress along the r - and φ -directions for each cross-section in Model-2 similar to that shown for Model-1 in figure 5. Figure 8(a) shows the cross-sections of the center of the heat region ($\varphi = 90^\circ$), Ω_{heat} , and of the neighboring region ($\varphi = 95^\circ$), Ω_{cool} . The thermal stress profiles, σ_r^{heat} along the r -direction and $\sigma_\varphi^{\text{heat}}$ along the φ -direction, were mapped at $T_{\text{max}} = 300$ K for each cross-section. Figures 8(b) and (c) show the σ_r^{heat} and $\sigma_\varphi^{\text{heat}}$ profiles in Ω_{heat} and figures 8(d) and (e) show the σ_r^{heat} and $\sigma_\varphi^{\text{heat}}$ profiles in Ω_{cool} , respectively.

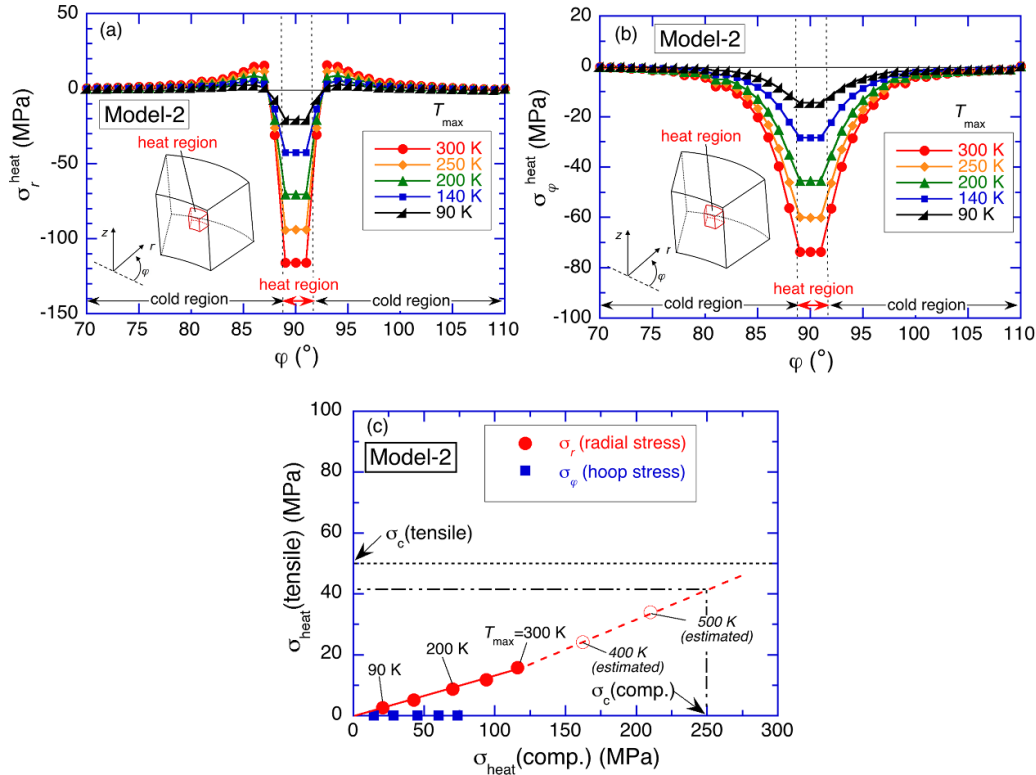


Figure 7. Angular (φ) dependence of thermal stress along (a) the r -direction, σ_r^{heat} , and (b) the φ -direction, $\sigma_\varphi^{\text{heat}}$, in the bulk ($x = 24$ mm, $z = 0$ mm) for each T_{max} for Model-2. (c) The relationship between the maximum thermal stress, $\sigma_{\text{heat}}^{\text{heat}}$, and the maximum thermal tensile stress, $\sigma_{\text{heat}}^{\text{heat}}$ (tensile), for σ_r^{heat} and $\sigma_\varphi^{\text{heat}}$ for each T_{max} . The data above 300 K are extrapolated to higher temperatures. The fracture strength in tension, $\sigma_c(\text{tensile}) = 50$ MPa, and in compression, $\sigma_c(\text{comp.}) = 250$ MPa, are indicated.

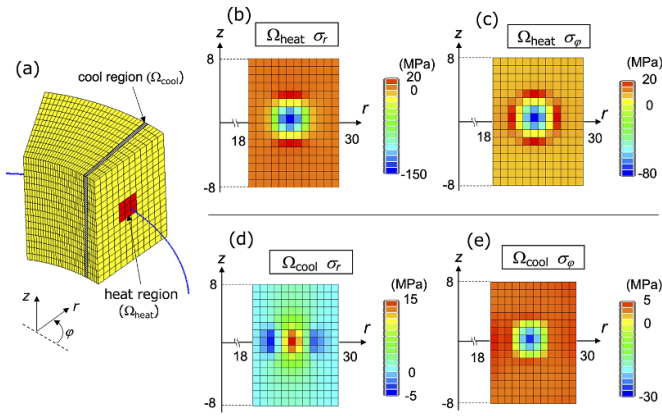


Figure 8. (a) Schematic view of the cross-sections of the center of the heat region ($\varphi = 90^\circ$), Ω_{heat} , and of the neighboring region ($\varphi = 95^\circ$), Ω_{cool} , for Model-2. The thermal stress profiles of (b) σ_r^{heat} and (c) $\sigma_\varphi^{\text{heat}}$ in Ω_{heat} . The thermal stress profiles of (d) σ_r^{heat} and (e) $\sigma_\varphi^{\text{heat}}$ in Ω_{cool} at $T_{\text{max}} = 300$ K for Model-2.

In figure 8(b), σ_r^{heat} in the small heat region ($\varphi = 90^\circ$), Ω_{heat} , indicates a compressive stress ($\sigma_r < 0$), but that outside of Ω_{heat} shows a small tensile value. On the other hand, σ_r^{heat} in the center of the neighboring region ($\varphi = 95^\circ$), Ω_{cool} , in figure 8(d) indicates a tensile stress, which reflects the existence of the small heat region at $\varphi = 89^\circ\text{--}92^\circ$. For the thermal stress along the φ -direction, the small compressive

stress for the small heat region and a small tensile stress for the neighboring region are generated at $\varphi = 90^\circ$, as shown in figure 8(c). These tendencies are weakened at $\varphi = 95^\circ$, as shown in figure 8(e). It should be noted that, contrary to Model-1 in figure 5, the stress increase was not observed at the corner of the heat region, because there are no open ends in the heat region in Model-2.

Finally, we consider which model reflects the real situation for the bulk fracture. Early in the ascending stage of PFM, magnetic flux intrudes from the outer surface of the bulk with small heat generation. After that, the dominant heat generation can take place due to a flux jump from a starting point such as voids, impurities and crystal defects. The realistic situation may be somewhere between Model-1 and Model-2, depending on the exact microstructure of the sample. On the other hand, Brandt pointed out numerically that the magnetic flux intrudes also from inner edge of a ring bulk of finite thickness [48]. This may create a sufficiently large temperature difference and stress near the inner edge for a crack to propagate from a local defect, resulting in the ring bulk fracture. In our study, the possibility of ring bulk fracture by thermal stress during PFM was suggested for a ring bulk with a large I.D, in which the ratio, ID/OD is 0.6. If the I.D. of the ring bulk is smaller, in which the bulk fracture was not reported for ID/OD = 0.4, for example in [13], the ‘C-shaped’ profile may arise as the result of local overheating and the destruction of superconductivity due to a flux jump. This idea is also applicable to superconducting

bulks magnetized by FCM, for which the cause of bulk fracture has been mainly considered only to be due to the electromagnetic hoop stress.

6. Conclusion

We have constructed two numerical models (Model-1 and Model-2) with different sizes of heat-generating region in a REBaCuO superconducting ring bulk and investigated the possibility of the mechanical fracture of the ring bulk due to thermal stress induced by local heat generation during PFM. Model-1 considers a large heat region and Model-2 considers a small heat region inside the bulk, in which the number of mesh elements is about 1/21 of that of Model-1. The valuable results and important conclusions of this study are summarized as follows.

- (a) For Model-1, the thermal stress along the radial and circumferential directions was compressive in nature in the heat region and tensile in nature in the neighboring region. The thermal stress increases with increasing induced heat Q (or maximum temperature, T_{\max}). The numerical analyses suggest that bulk fracture inside the bulk due to the thermal stress results from the tensile stress along the r -direction in the neighboring region.
- (b) In Model-1, open ends exist in the heat region along the z - and r -directions. The thermal stress at the open ends in the heat region was also investigated. The risk of bulk fracture is enhanced at the inner or outer edges of the bulk surface, compared with inside the bulk. The ring bulk is easy to break from the surface edge under the assumptions of Model-1.
- (c) For Model-2, the thermal stress, σ_r^{heat} , along the radial direction was compressive in the heat region and tensile in the neighboring region. However, the thermal stress, $\sigma_\varphi^{\text{heat}}$, along the circumferential direction was also compressive, which is larger than that of Model-1, in the heat region, but was nearly zero along the circumferential direction in the neighboring region. The numerical analyses using Model-2 suggest that the fracture inside the bulk due to the thermal stress results from the compressive stress along the radial direction in the neighboring region.
- (d) Up to now, the bulk fracture in the ring bulk during magnetizing process has been mainly considered to result from the electromagnetic stress. However, the electromagnetic stress alone may not account for the ring bulk fracture during PFM, as suggested by our numerical simulations: the possibility of mechanical fracture of a ring bulk due to thermal stress induced by local heat generation. This concept is also applicable more generally to the fracture mechanism during FCM of ring/disk superconducting bulks.

Data availability statement

All data that support the findings of this study are included within the article (and any supplementary files).

Acknowledgments

This new concept of thermal stress origin started from discussion for the mechanical fracture of the disk bulk during FCM between the author (H.F.) and Prtof. Tomoyuki Naito (T.N.) of Iwate University in 2018. H.F. thanks T.N. for valuable suggestions. The authors thank Mr Michael Beck of the University of Cambridge for valuable discussions. This research is supported by JSPS KAKENHI Grant No. 19K05240, and by Adaptable and Seamless Technology transfer Program through Target-driven R&D (A-STEP) from Japan Science and Technology Agency (JST), Grant Nos. VP30218088419 and JPMJTM20AK. M D Ainslie would like to acknowledge financial support from an Engineering and Physical Sciences Research Council (EPSRC) Early Career Fellowship, EP/P020313/1. All data are provided in full in the results section of this paper.

ORCID iDs

Hiroyuki Fujishiro  <https://orcid.org/0000-0003-1483-835X>

Keita Takahashi  <https://orcid.org/0000-0002-8278-2688>

Mark D Ainslie  <https://orcid.org/0000-0003-0466-3680>

References

- [1] Durrell J H, Ainslie M D, Zhou D, Vanderbemden P, Bradshaw T, Speller S, Filipenko M and Cardwell D A 2018 *Supercond. Sci. Technol.* **31** 103501
- [2] Yokoyama K, Oka T, Okada H, Fujine Y, Chiba A and Noto K 2003 *IEEE Trans. Appl. Supercond.* **13** 7711238
- [3] Nakamura T, Tamada D, Yanagi Y, Itoh Y, Nemoto T, Utsumi H and Kose K 2015 *J. Magn. Reson.* **259** 68–75
- [4] Tomita M and Murakami M 2003 *Nature* **421** 517–20
- [5] Durrell J H et al 2014 *Supercond. Sci. Technol.* **27** 082001
- [6] Huang K-Y et al 2020 *Supercond. Sci. Technol.* **33** 02LT01
- [7] Ikuta H, Yanagi Y, Yoshikawa M, Itoh Y, Oka T and Mizutani U 2001 *Physica C* **357–360** 837
- [8] Sander M, Sutter U, Koch R and Klaser M 2000 *Supercond. Sci. Technol.* **13** 841
- [9] Fujishiro H, Tateiwa T, Fujiwara A, Oka T and Hayashi H 2005 *Physica C* **445–448** 334–8
- [10] Zhou D, Ainslie M D, Srđič J, Huang K, Shi Y H, Dennis A R, Cardwell D A, Durrell J H, Boll M and Filipenko M 2018 *Supercond. Sci. Technol.* **31** 105005
- [11] Ohsaki H, Shimosaki T and Nozawa N 2002 *Supercond. Sci. Technol.* **15** 754–8
- [12] Krasnoplenov E P, Korotkov V S and Kartamyshev A A 2017 *Tech. Phys. Lett.* **43** 882–4
- [13] Zhou D, Shi Y H, Dennis A R, Cardwell D A and Durrell J H 2020 *Supercond. Sci. Technol.* **33** 034001
- [14] Fujimoto H, Murakami A, Teshima H and Morita M 2013 *Cryogenics* **57** 6–11
- [15] Konstantopoulou K, Shi Y H, Dennis A R, Durrell J H, Pastor J Y and Cardwell D A 2014 *Supercond. Sci. Technol.* **27** 115011
- [16] Huang K Y et al 2018 *IEEE Trans. Appl. Supercond.* **28** 6801505
- [17] Sakai N, Mase A, Ikuta H, Seo S J, Mizutani U and Murakami M 2000 *Supercond. Sci. Technol.* **13** 770–3
- [18] Murakami A et al 2003 *Cryogenics* **43** 345–50

- [19] Fujishiro H, Naito T and Awaji S 2019 *Supercond. Sci. Technol.* **32** 045005
- [20] Kan R, Katagiri K, Murakami A, Kasaba K, Shoji Y, Noto K, Sakai N and Murakami M 2004 *IEEE Trans. Appl. Supercond.* **14** 8132078
- [21] Murakami A, Katagiri K, Kan R, Miyata H, Shoji Y, Noto K, Iwamoto A and Mito T 2005 *Physica C* **426–431** 644–8
- [22] Mochizuki H, Fujishiro H, Naito T, Itoh Y, Yanagi Y and Nakamura T 2016 *IEEE Trans. Appl. Supercond.* **26** 6800205
- [23] Johansen T H 1999 *Phys. Rev. B* **60** 9690
- [24] Johansen T H, Wang C, Chen Q Y and Chu W-K 2000 *J. Appl. Phys.* **88** 2730–3
- [25] Johansen T H 2000 *Supercond. Sci. Technol.* **13** R121
- [26] Fujishiro H, Ainslie M D, Takahashi K, Naito T, Yanagi Y, Itoh Y and Nakamura T 2017 *Supercond. Sci. Technol.* **30** 085008
- [27] Takahashi K, Fujishiro H, Naito T, Yanagi Y, Itoh Y and Nakamura T 2017 *Supercond. Sci. Technol.* **30** 115006
- [28] Fujishiro H, Naito T, Yanagi Y, Itoh Y and Nakamura T 2019 *Supercond. Sci. Technol.* **32** 065001
- [29] Ainslie M D, Huang K Y, Fujishiro H, Chaddock J, Takahashi K, Namba S, Cardwell D A and Durrell J H 2019 *Supercond. Sci. Technol.* **32** 034002
- [30] Wu H, Yong H and Zhou Y 2018 *Supercond. Sci. Technol.* **31** 045008
- [31] Ru Y, Yong H and Zhou Y 2019 *Supercond. Sci. Technol.* **32** 074001
- [32] Wu H, Yong H and Zhou Y 2020 *Supercond. Sci. Technol.* **33** 124002
- [33] Zhang M, Matsuda K and Coombs T A 2012 *J. Appl. Phys.* **112** 043912
- [34] Jing Z 2020 *Supercond. Sci. Technol.* **33** 075009
- [35] Hirano T, Fujishiro H, Naito T and Ainslie M D 2020 *Supercond. Sci. Technol.* **33** 044003
- [36] Ainslie M D, Fujishiro H, Ujiie T, Zou J, Dennis A, Shi Y H and Cardwell D A 2014 *Supercond. Sci. Technol.* **27** 065008
- [37] Namba S, Fujishiro H, Naito T, Ainslie M D and Huang K Y 2019 *Supercond. Sci. Technol.* **32** 125011
- [38] Shimoyashiki F, Fujishiro H, Hirano T, Naito T and Ainslie M D 2020 *J. Phys.: Conf. Ser.* **1559** 012029
- [39] Ainslie M D, Fujishiro H, Mochizuki H, Takahashi K, Shi Y H, Namburi D K, Zou J, Zhou D, Dennis A R and Cardwell D A 2016 *Supercond. Sci. Technol.* **29** 074003
- [40] Shinden M, Namba S, Hirano T, Fujishiro H, Naito T and Ainslie M D 2020 *J. Phys.: Conf. Ser.* **1550** 012048
- [41] Korotkov V S, Krasnoperov E P and Kartamyshev A A 2017 *Supercond. Sci. Technol.* **30** 095004
- [42] Korotkov V S, Krasnoperov E P and Kartamyshev A A 2016 *J. Phys.: Conf. Ser.* **695** 012007
- [43] Grover F 1973 *Inductance Calculations: Working Formulas and Tables* (New York: Dover) p 105
- [44] Brazhnik P A and Krasnoperov E P 2021 *J. Supercond. Novel Magn.* **34** 1085–90
- [45] Zhang Z Y, Matsumoto S, Choi Y S, Teranishi R and Kiyoshi T 2011 *Physica C* **471** 1547
- [46] Takahashi K, Fujishiro H and Ainslie M D 2018 *Supercond. Sci. Technol.* **31** 044005
- [47] Takahashi K, Fujishiro H, Namba S and Ainslie D 2021 *Supercond. Sci. Technol.* **34** 05LT02
- [48] Brandt E H 1997 *Phys. Rev. B* **55** 14513